Chinese Chemical Letters 35 (2024) 108286

Contents lists available at ScienceDirect

Chinese Chemical Letters

journal homepage: www.elsevier.com/locate/cclet

Two-dimensional transition metal MXene-based gas sensors: A review

Junfeng Li[a,1,*], Xiaojie Chen[a,1], Xiaojie Zhu[a], Yingchang Jiang[b], Xueting Chang[b], Shibin Sun[a,*]

[a] College of Logistics and Engineering, Shanghai Maritime University, Shanghai 201306, China
[b] Institute of Marine Materials Science and Engineering, Shanghai Maritime University, Shanghai 201306, China

ARTICLE INFO

Article history:
Received 21 October 2022
Revised 21 December 2022
Accepted 1 March 2023
Available online 4 March 2023

Keywords:
MXene
Gas sensors
Synthesis
Stability
Gas-sensing mechanism
Gas-sensing performance

ABSTRACT

As an emerging star in the family of two-dimensional (2D) materials, 2D transition metal carbides, carbonitrides and nitrides, collectively referred to as MXenes, have large specific surface area, rich active sites, metallic conductivity and adjustable surface chemical properties. These features make MXenes promising candidates for gas-sensing materials. For the past few years, MXene-based sensors have drawn increasing attention due to their enhanced sensor performance. Based on this, this review systematically represents the structure, synthesis methods and properties of MXenes, and summarizes their applications in gas sensors. Firstly, the types, structure, main synthesis methods and properties of MXenes are introduced in a comprehensive way. Next, the corresponding design principle and working mechanism of MXene-based gas sensor are clarified. Subsequently, the sensing performances of pristine MXenes and the MXene-based nanocomposite are discussed. Finally, some future opportunities and challenges of MXene-based sensors are pointed out.

1. Introduction

Gas sensors are essential for monitoring of environmental health in real time [1–3]. Air quality monitoring is driving the market of gas sensors. According to verifiable market research conducted by BBC Research, the worldwide market for gas sensors had a value of USD 999.36 million in 2019 and is expected to reach USD 1642.46 million by 2027, expanding at a compound annual growth rate (CAGR) of 6.91% from 2020 to 2027 [4]. The application fields of gas sensors include industrial production, food safety, medical diagnosis, environmental monitoring, intelligence home as well as national security [5–9]. The function of gas sensors is to convert gas composition and concentration into electrical signals that can be measured. The ultimate goal of research is to develop gas-sensing materials with high sensitivity, selectivity, stability and fast response, low power consumption, and low cost. Achieving all of the above goals is very difficult, and researchers must balance performance trade-offs. Various types of gas sensing materials have been found, such as metal oxide [10–12], conductive polymer [13–15], carbon-based nanomaterials [16], and 2D materials [17–20]. Metal oxides semiconductor (MOS) are the most widely used in gas sensors. In recent years, various strategies have been developed to improve the gas sensing performance of MOS, such as oxygen vacancy construction. The existence of oxygen vacancy could effectively tune the surface redox reactivity and charge carrier mobility [21–23]. However, the gas molecules' adsorption and desorption of MOS sensors need to be promoted by heating to change the conductive properties of the sensors (such as resistance), thereby realizing the purpose of gas detection [24]. The optimal operating temperature of metal oxide semiconductors generally exceeds 180 degrees, which brings greater power loss and the risk of igniting flammable gases [25–29]. Therefore, it is imperative to develop gas-sensing materials with low detection limit that can work at room temperature.

$M_{n+1}AX_n$ is a ternary layered ceramic material, where M represents early transition metals, such as Sc, Ti, Zr, Cr and Co. A includes IIIA or IVA elements, such as Al, Si, Ga, Ge, In and Sn. X refers to C and/or N, $n = 1$, 2, 3 or 4 [30,31]. The crystal structure of the MAX phase is layered hexagonal with the space group being $P6_3/mmc$. The X atoms occupy the center of the octahedron of the M atomic layer, and the A atomic layers are alternately arranged in the octahedron. 2D transition metal carbides, carbonitrides and nitrides, collectively referred to as MXenes, are recently discovered by selectively etching the A atomic layer from the MAX phase. MXene takes its name from MAX phase and its graphene-like properties. The general chemical formula is $M_{n+1}X_nT_x$, where M represents the transition metal elements, X refers to C or N,

* Corresponding authors.
E-mail addresses: jfli@shmtu.edu.cn (J. Li), sunshibin@shmtu.edu.cn (S. Sun).
[1] These authors contributed equally to this work.

https://doi.org/10.1016/j.cclet.2023.108286
1001-8417/

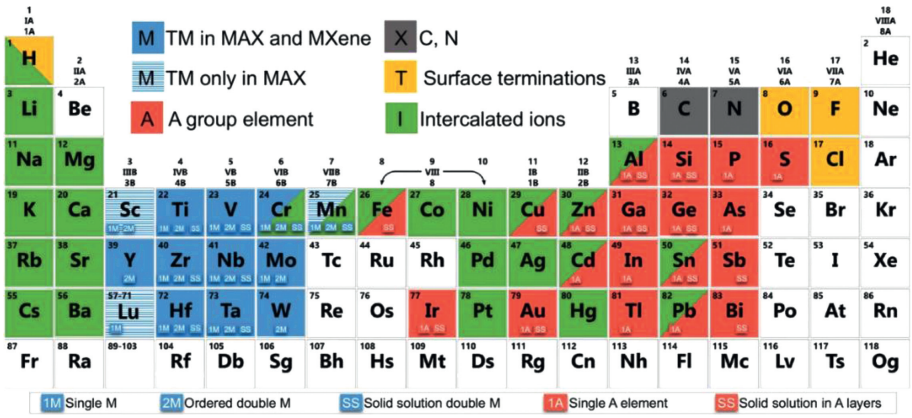

Fig. 1. Periodic table showing the elements in MAX phases and MXenes, surface terminations and intercalant cations based on experimental studies. Reprinted with permission [31]. Copyright 2019, Springer Nature.

n is generally 1-4, and T_x indicates surface groups (such as O^{2-}, OH^- and F^-) [32]. In Fig. 1, the reported surface terminations are highlighted in yellow and the transition metals in blue. Specifically, transition metals (TM) in both MAX and MXenes are in solid blue, while TMs only in MAX in blue with horizontal stripes (Sc, Lu and Mn). More than 30 different MXenes have been prepared in the laboratory and more than 100 theoretically predicted MXenes have different physical and chemical properties [33,34]. Additionally, the formation of diverse solid solutions and the possibility of surface termination make MXenes large and diverse in the family of 2D materials. MXenes have been applied extensively in many fields, like energy storage devices [35,36], photovoltaic cells [37], lithium-sulfur batteries [38,39], biomedical applications [40,41], superapacitors [42], humidity sensing [43], and environment-related applications [44].

According to the chemical composition and crystal structure of the material, MXenes are divided into three categories: (1) A single transition metal with only one transition metal M and no vacancy structure, denoted by the formula: $M_{n+1}X_nT_x$. (2) The solid solution double transition metal with disordered distribution of M' and M" in the same plane [45]. The distribution has no regularity. It is recorded as the formula: $(M'M")_{n+1}X_nT_x$, such as TiVC, TiNbC, VNbC, $(Ti_{0.7}V_{0.3})_2C$. (3) Ordered double transition metals: (i) If M' and M" can be independent on their respective atomic planes, forming a non-independent plane order, called *o*-MXene, the formula: $(M'_2M")X_2T_x$ or $(M'_2M"_2)$ XT_x such as: MoTiC. (ii) If two transition metals have planar order in the same layer and form alternating M' and M" atoms, called i-MXene, M" atoms will be etched during the etching process, resulting in ordered vacancies, denoted $M'_{1.33}XT_x$, such as $Mo_{1.33}C$ and $Nb_{1.33}C$ [32]. In Fig. 1, SS represents the existence of solid solutions in transition metal atomic planes (marked blue) or A-element planes (marked red). 1M and 1A represent the possibility of a single transition metal and A-element MAX phase (and MXene) formation for those specific elements. 2M represents the formation possibility of an ordered double transition metal MAX phase. The green background shows the cations intercalated into MXenes. The structures of MXenes were shown in Fig. 2.

The physical properties of MXene are relatively scarce, especially for multilayer MXene. In general, theoretical research is based on single-layer MXene. The effective Young's modulus of 0.98 nm monolayer $Ti_3C_2T_x$ MXene film was reported in the laboratory to be 333±30 GPa with the 17.3±1.6 GPa breaking strength [46]. According to molecular dynamics simulations, the Young's modulus of Ti_3C_2 is 502 GPa [47]. This is due to the presence of surface functionalization and defects, resulting in a lower value determined experimentally. Furthermore, both the in-plane stiffness and out-of-plane bending stiffness of MXene are fundamental parameters of its mechanical properties. By first-principles calculations, Hu *et al.* drew several important conclusions [48]: (1) In-plane stiffness increases with atomic layers. (2) Surface functional groups have a certain impact on in-plane stiffness, and oxygen functional groups will increase in-plane stiffness relatively. (3) The bending stiffness of single-layer MXene is much higher than that of graphene, which is about 3-130 times that of graphene. (4) Flexibility of MXenes decreases as the layer thickness increases. Thinnest MXenes show better flexibility but the in-plane stiffness reduces. The electrical properties of MXene are affected by its elemental composition. As a polyatomic composition material, each part has effect on electrical conductivity. If the transition element is different, the conductivity will be different. In addition, nitride and carbonitride MXenes are more conductive than carbide MXenes [49]. Finally, the electrical conductivity of MXene is also in relation to surface functional groups, defects, number of layers and thickness. Surface modification by heat treatment and intercalation alkali treatment could be an effective approach to improve the electrical properties, whose experimental results show that the electrical conductivity is increased by two orders of magnitude [50].

Notably, MXenes have drawn increasing attention in the sensor field for their high metallic conductivity, hydrophilicity, and large specific surface area. Therefore, MXenes are regarded as revolutionary 2D materials and expected to go beyond the boundaries of existing sensor technologies, serving as alternative sensor materials.

2. Synthesis of MXenes

The synthetic method has a determining impact on the properties of MXene. The MXene obtained after selective etching is generally a multi-layer two-dimensional material, and after simple ultrasonic treatment, the multi-layer MXene can be exfoliated to obtain MXene nanosheets with single-layer or few-layer [51]. Unlike the weak van der Waals forces between carbon atoms in graphene, the strong M-X bonds in the MAX phase have mixed covalent/metallic/ionic properties and the M-A bonds are metallic ones, so the MAX phase cannot be sheared or other similar mechanical method destroyed [52]. Since the M-X bond and the M-A bond have different bonding strengths, this can be used to selectively break the M-A bond to etch the A layer while retaining the M-X bond. The $M_{n+1}X_n$ surface obtained after etching has high chemical activity, and it is easy to form $M_{n+1}X_nT_x$ with surface functional groups. After selectively etching the A atomic layer from the MAX phase, the ions in solution such as hydroxyl and fluoride ions, will combine with the unsaturated MX layer to form vari-

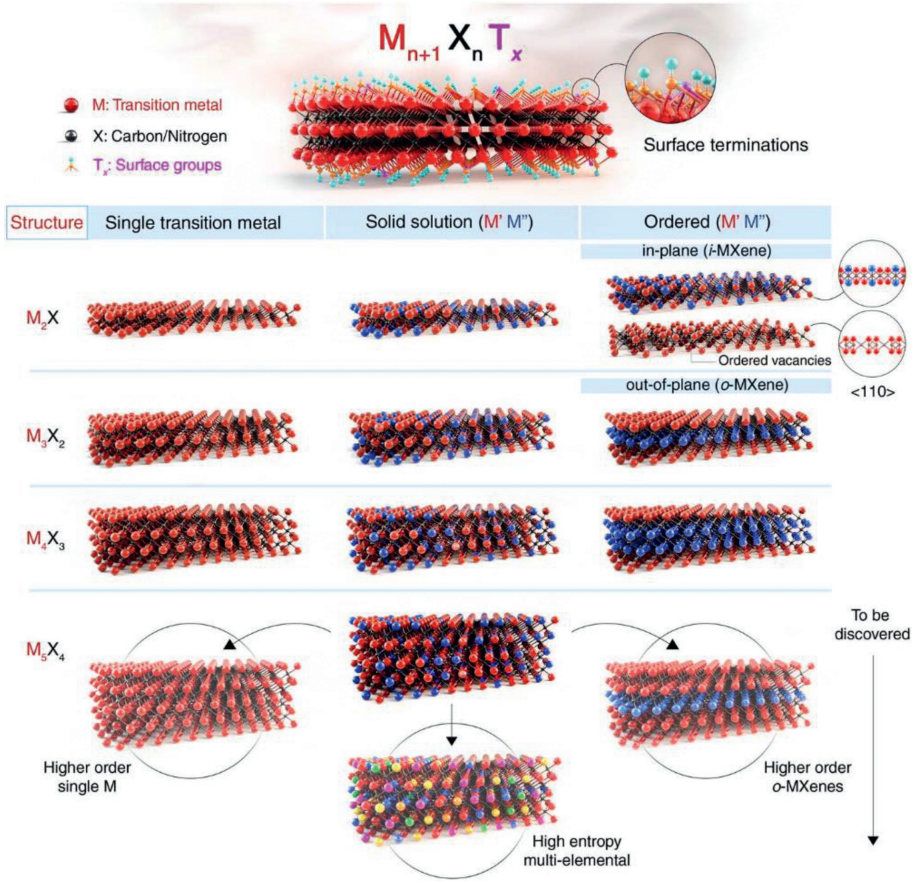

Fig. 2. Schematic illustration of the MXene structures. Reprinted with permission [32]. Copyright 2021, American Association for the Advancement of Science.

ous functional groups. Different etching environments will lead to the existence of different types and numbers of functional groups on the MXenes surface, affecting the surface hydrophilicity, ion adsorption and diffusion speed of MXenes materials. In fact, the surface functional groups of MXene can also be tuned by various strategies, such as Lewis-basic halides treatment, substitution and elimination reactions in molten inorganic salts [53,54]. The surface functional groups in MXene offers possibilities for surface state engineering and regulation of band structure and electrical properties. For instance, a large number of hydroxyl groups could effectively enhance the hydrophily of MXene.

2.1. Hydrofluoric acid etching

As we all know, 2011 is the first year of MXene. Yury Gogotsi *et al.* discovered the preparation of $Ti_3C_2T_x$ by selectively etching the Al layer in the MAX material Ti_3AlC_2 material using hydrofluoric acid (HF) at room temperature [55]. Having immersed about 10 g of Ti_3AlC_2 powder in about 100 mL of a 50% concentrated HF solution for 2 h at room temperature, they decided to name it as "MXene" to emphasize its graphene-like morphology. By *ab initio* simulation, they predicted that the characteristics of MXene could be modified by altering the surface terminations. Fig. 3a shows the etching mechanism. Fig. 3b shows the XRD patterns of the samples before and after etching. In reaction with HF etchant, the characteristic Ti_3AlC_2 peak located at 39° disappeared, demonstrating the etching of MAX completed. $Ti_3C_2T_x$ was the first member of MXenes family, immediately after the second year more MXenes were synthesized by etching with HF, such as Ti_2C, Ta_4C_3, TiNbC, $(V_{0.5},Cr_{0.5})_3C_2$ and Ti_3CN_x [51]. They all came from Al-containing MAX phase, such as Ti_2AlC, and Ta_4AlC_3. The morphologies of the Ti_3AlC_2 MAX phase and the above five Al-containing MAX derivate are shown in Fig. 3d. As seen, all the products reveal an accordion-like multilayer structure, proving the universality of HF in etching the Al-containing MAX phases. Since then, many more MXenes were successfully prepared by etching their precursor Al-containing MAX phases, *e.g.*, V_4C_3, V_2C, Nb_4C_3, Mo_4VC_4 and Cr_2C [56–60]. Based on the above research results, for the Al-containing MAX phase, the operative reactions are presumed to be:

$$M_{n+1}AlX_n + 3HF = AlF_3 + M_{n+1}X_n + 1.5H_2 \quad (1)$$

$$M_{n+1}X_n + 2H_2O = M_{n+1}X_n\ (OH)_2 + H_2 \quad (2)$$

$$M_{n+1}X_n + 2HF = M_{n+1}X_n\ F_2 + H_2 \quad (3)$$

Reaction 1 indicates the generation of $M_{n+1}X_n$ layers from $M_{n+1}AlX_n$, and Reactions 2 and/or 3 reveal the formation of surface terminations (–OH and–F) on $M_{n+1}X_n$. The experimental results show that the above-mentioned materials are immersed in different concentrations of hydrofluoric acid solution for different times, the concentration range is 10-50 wt%, and the time range is 10-72 hours. To investigate the effect of hydrofluoric acid concentration, reaction time and operation temperature on the final product, Alhabeb *et al.* used HF etchant with different concentrations and time periods to etch Ti_3AlC_2 at room temperature [61]. Their experiment revealed that the etching time was shorten by

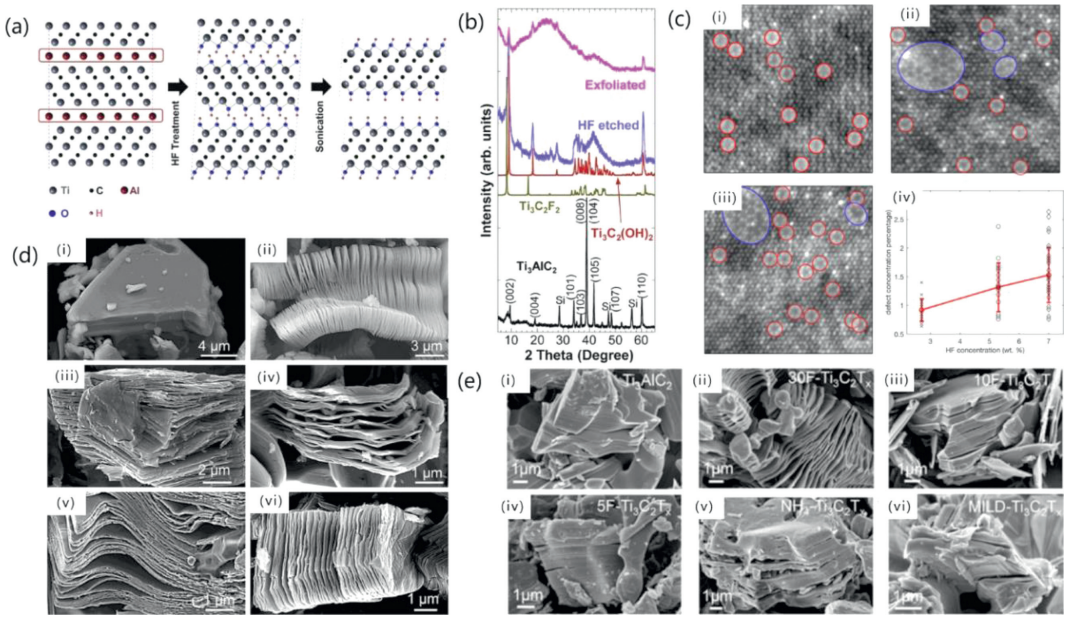

Fig. 3. (a) $Ti_3C_2T_x$ obtained from the MAX phase etching by HF. (b) XRD pattern for Ti_3AlC_2, $Ti_3C_2F_2$ and $Ti_3C_2(OH)_2$. Reprinted with permission [55]. Copyright 2011, Wiley-VCH Verlag GmbH & Co. KGaA, Weinheim. (c) $Ti_3C_2T_x$ MXene flakes prepared using different HF concentrations and scatter plot of defect concentration from images. Reprinted with permission [62]. Copyright 2016, American Chemical Society. (d) (i) Ti_3AlC_2 particle before HF treatment and (ii) Ti_3AlC_2, (iii) Ti_2AlC, (iv) Ta_4AlC_3, (v) TiNbAlC, and (vi) Ti_3AlCN after HF treatment. Reprinted with permission [51]. Copyright 2012, American Chemical Society. (e) (i) Ti_3AlC_2 (MAX) powder, (ii-iv) multilayered $Ti_3C_2T_x$ powder synthesized with different HF concentrations, (v) multilayered NH_4-$Ti_3C_2T_x$ and (vi) MILD-$Ti_3C_2T_x$ powder. Reprinted with permission [61]. Copyright 2017, American Chemical Society.

higher HF concentration, as shown in Fig. 3e. Increasing the concentration of hydrofluoric acid can indeed improve the synthesis efficiency, but it also produces more surface defects and smaller flake size [62]. Fig. 3c shows $Ti_3C_2T_x$ prepared using etchants with different HF concentrations. After etching with a concentration of 2.7 wt% HF, vacancy clusters were detected seldom, but after etching with a concentration of 7 wt% HF, vacancy clusters were observed often. We should selectively change the experimental conditions according to the desired properties and application to control the size and number of defects in the product. MXenes of large flake size with few defects are more suitable for optics, electronics, and electromagnetism application. Comparatively, MXenes of small flake size and few defects are more suitable for catalysis and gas sensing applications, providing basis for strengthening the application of MXene in gas sensors.

The etching condition for one transition metal in Al-containing MAX phases vary from another in terms of the structure, atomic bonding and particle size of the material [35]. Many studies have shown that the hydrofluoric acid concentration, etching time, and etching temperature required to prepare different MXenes are different [63,64]. Two parameters need to be focused on to discuss the stability of MAX materials. One is the atomic number of M that makes up the M-Al chemical bond, and the other parameter is the value of *n*. On the one hand, the atomic number of M is different, and so is the bond energy of M-A in the MAX phase. To be specific, the larger the atomic number of M is, the greater the bond energy of M-A is. For example, the bond energies of Nb-Al in Nb_2AlC are larger than the bond energies of Ti-Al in Ti_2AlC [65]. Therefore, the etching of the Al layer in Nb_2AlC requires longer time or higher HF concentration than Ti_2AlC [51,66]. On the other hand, in $M_{n+1}X_nT_x$, the larger the *n* value, the better the stability of MAX, and the longer time or higher HF concentration is required [34]. For instance, immersing Ti_2AlC powders in 50% HF resulted in their complete dissolution, but Ti_3C_2 was yielded in the same conditions. Ti_2C can only be obtained from Ti_2AlC by decreasing the concentration of HF from 50% to 10% [51].

2.2. In situ HF etching

In view of the strong corrosiveness and relatively high cost of hydrofluoric acid, researchers began to look for milder and more economical etchants. To avoid the direct use of hydrofluoric acid, a method to generate HF *in situ* using fluoride salts (such as LiF, Na, and KF) mixed with strong acids (such as HCl and H_2SO_4) was developed. In 2014, Ghidiu *et al.* found out a producing method of this material by virtue of a solution of lithium fluoride and hydrochloric acid [67]. The synthetic route is shown in Fig. 4a. As shown in Fig. 4b, the resulting hydrophilic material swelled when hydrated and could be shaped like clay and dried into a highly conductive solid or rolled into films tens of micrometers thick. The advantage of this method is that the positive ions of fluorine salt species will intercalate into the MXene layer during the etching process, which will assist in the subsequent ultrasonic process. It is convenient to obtain single-layer MXene. This method marks the success of etching using low-concentration hydrofluoric acid, and at the same time plays a role in reducing environmental pollution. Lipatov *et al.* conducted experiments using two routes by adjusting the different ratios of LiF to MAX phases, finding out when the ratio of LiF to Ti_3AlC_2 was 7.5:1, the produced $Ti_3C_2T_x$ flakes were significantly higher in both quality and size (Figs. 4c and d) [68]. In addition, the prepared ML-MXene can be directly separated into monolayers by hand shaking without sonication. Moreover, a single $Ti_3C_2T_x$ flake exhibits high electrical conductivity and field-effect electron mobility, and remains quite stable and excellent even after being exposed to air for more than 24 h. Besides LiF, other fluoride salts have also been used in this method. Presented by Liu *et al.* was the preparation of Ti_3C_2 MXene and Ti_2C MXene by etching Ti_3AlC_2 and Ti_2AlC with various fluoride salts in HCl, LiF, NaF, KF and NH_4F [69]. In Fig. 4e, scanning electron

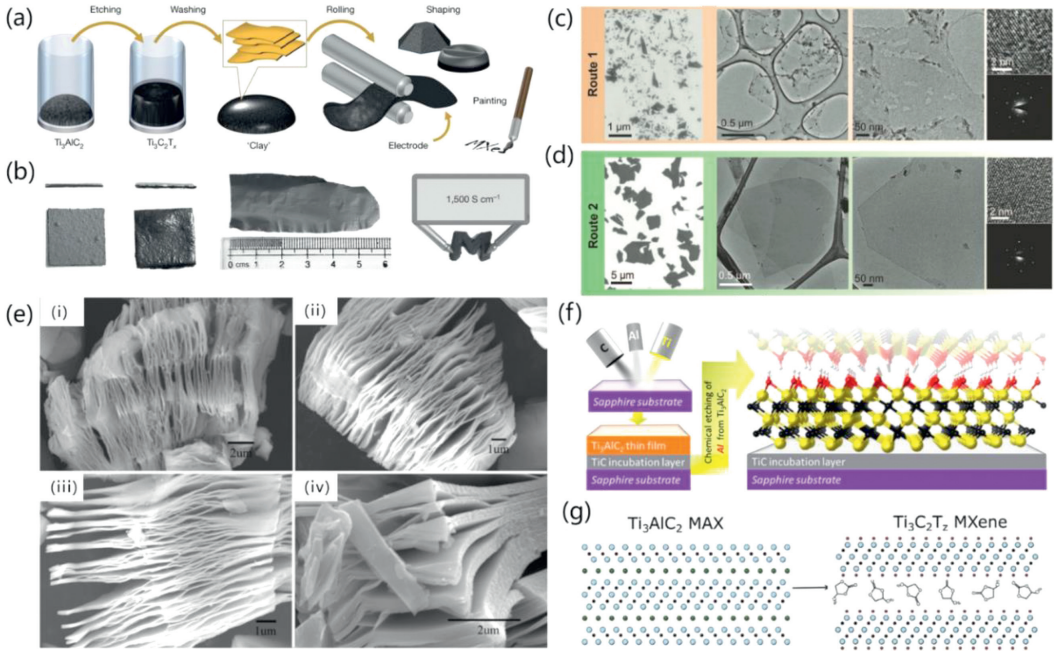

Fig. 4. (a, b) Schematic of MXene synthesis and electrode preparation. Reprinted with permission [67]. Copyright 2014, Nature Publishing Group, a division of Macmillan Publishers Limited. (c) $Ti_3C_2T_x$ and (d) $Ti_3C_2T_x$ flakes produced using route 1 and route 2, respectively. Reprinted with permission [68]. Copyright 2011, Wiley-VCH Verlag GmbH & Co. KGaA, Weinheim. (e) Ti_2AlC exfoliated by different fluoride salts respectively. Reprinted with permission [69]. Copyright 2017, Elsevier B.V. (f) Steps used to produce epitaxial MXene films by magnetron sputtering. Reprinted with permission [70]. Copyright 2014, American Chemical Society. (g) Abridged version schematic of synthesis. Reprinted with permission [72]. Copyright 2020, Elsevier Inc.

microscope (SEM) images of Ti_3C_2 are shown. According to the results of tests on the adsorption of methane by MXenes made from LiF and NH_4F, these MXenes can absorb methane under high pressure and can maintain methane under normal pressure. As a result, these MXenes may have important applications in the sensing of methane or other hazardous gas molecules. The different adsorption characteristics of MXenes may be traced, at least in part, to the different surface structures of the MXenes in question. According to a theoretical calculation and the findings of XPS, the surface structure of produced MXene is affected by the kind of positive ions (Li^+, Na^+, K^+, or NH_4^+) that are present in the etchant solution.

In addition to fluoride, hydrogen fluoride has also been shown to be an effective etchant. In fact, hydrogen fluoride was reported earlier in the same year as LiF was reported. Halim *et al.* readily made a sort of transparent conductive two-dimensional titanium carbide epitaxial thin films at room temperature [70]. The synthesis process is shown in Fig. 4f. Due to the intercalation with NH_3 and NH_4^+, products synthesized from hydrogen fluoride have c lattice parameters (~25 Å) that are 25% larger than films etched with HF. Larger interlayer distance means greater specific surface area, which should be beneficial for its sensing performance. The large interlayer could not only enhance the surface to volume ratio and make active sites greater, but also make ion transport wider, which should be beneficial for its sensing performance. For example, Kim *et al.* reported that the enlarged interlayer spacing effectively showed a much higher signal-to-noise ratio upon exposure to analytes [71]. Most of the reported etching methods are carried out in aqueous solution. Naturt *et al.* creatively used an water-free etching method, the etchant used is hydrogen fluoride, and the etching process takes place in an organic polar solution [72]. A brief synthetic route is shown in Fig. 4g. They further presented the possibility of obtaining $Ti_3C_2T_x$ flakes rich influorine terminations by using this etching method. The electrodes made from $Ti_3C_2T_x$ etched in certain organic solutions such as propylene carbonate resulted in Na-ion battery anodes with double the capacity to those etched in water.

2.3. Molten salt etching

Carbides are frequently reported MXenes, but nitrides are rarely reported, which is attributed to the different chemical properties of the nitride MAX phase from that of carbide MAX. Neither conventional hydrofluoric acid nor *in situ* HF generation methods can prepare nitride MXenes. Until 2016, Urbankowski *et al.* used a special etching method to successfully prepare Ti_4N_3 from Ti_4AlN_3 [73]. Fig. 5a depicts a schematic diagram of the synthesis and layering process of $Ti_4N_3T_x$. However, at present, this method is only applicable to the preparation of $Ti_4N_3T_x$ MXene. Whether it can be used for the preparation of other MXenes is still unknown. At the same time, the corrosion of fluoride salt to equipment is serious under high temperature conditions, which also restricts the large-scale promotion of this preparation method.

The fluorine-containing compound etching method leads to the inevitable F functional group on the surface of the synthesized product, which not only affects the application of the material in some aspects, such as supercapacitors and lithium-ion batteries, but also do certain harm to environment. Li *et al.* provide a broad strategy for the synthesis of a series of Zn-based MAX phases and Cl-terminated MXenes, which originate from the replacement reaction between the MAX phase and the late transition-metal halides [74]. The etching action of Lewis acid in molten salts offers a green and practical technique to synthesizing MXenes using an HF-free chemical procedure. This is the first time that only Cl-terminated MXenes have been created.

Li *et al.* produced a variety of MXenes using unorthodox MAX phase precursors including Si, Zn and Ga [75]. They also developed and confirmed redox-controlled A-site etching of MAX phases in Lewis acidic melts. A diagram of the $Ti_3C_2T_x$ MXene synthesis from the reaction of Ti_3SiC_2 and $CuCl_2$ at 750 °C is shown in Fig. 5b.

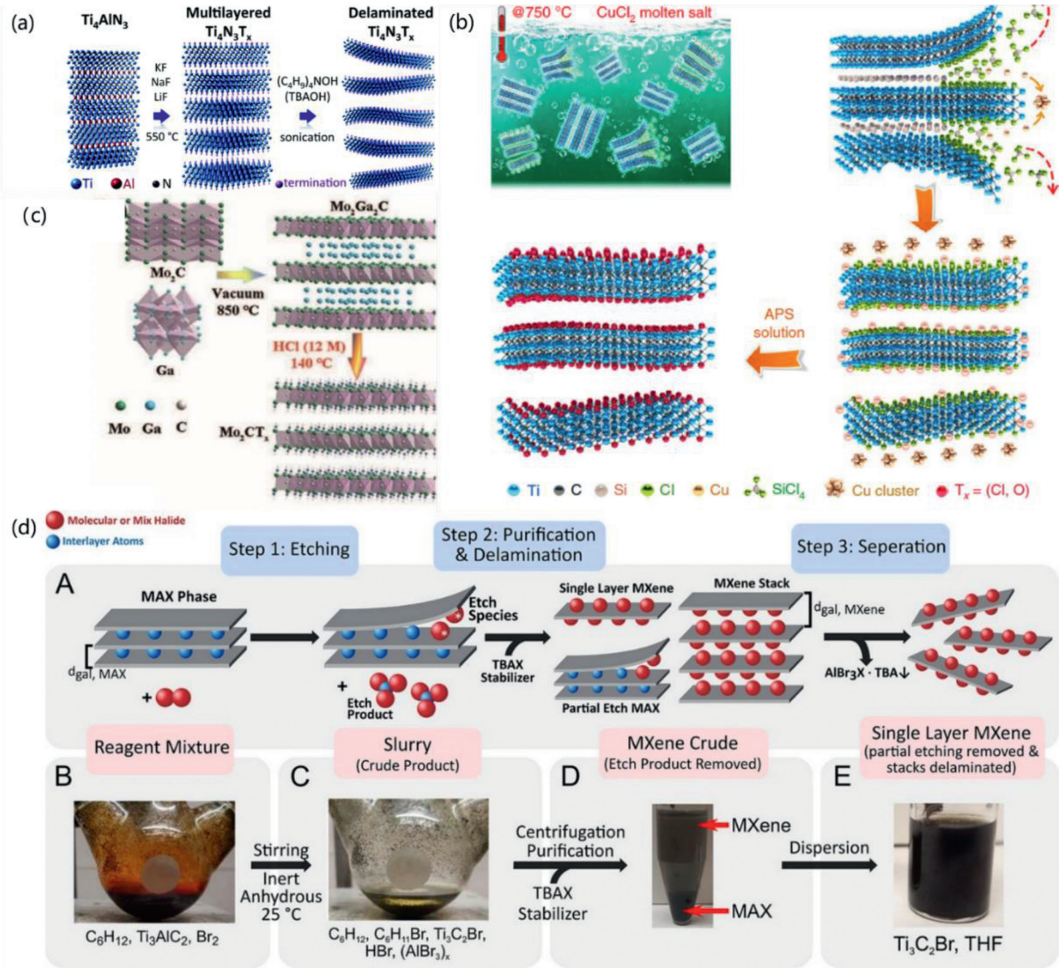

Fig. 5. (a) Schematic illustration of the synthesis of $Ti_4N_3T_x$. Reprinted with permission [73]. Copyright 2016, Royal Society of Chemistry. (b) Schematic illustration of the synthesis of $Ti_3C_2T_x$. Reprinted with permission [75]. Copyright 2020, Springer Nature. (c) Schematic illustration of the preparation procedure for fluoride-free Mo_2CT_x. Reprinted with permission [77]. Copyright 2021, Wiley-VCH GmbH. (d) Schematic of halogen etch of MAX phases. Reprinted with permission [78]. Copyright 2021, American Chemical Society.

This molten salt synthesis process yields an anode of Ti_3C_2 MXene material with a Li^+ storage capacity of up to 738 C/g and a high charge-discharge rate. The speical molten salt preparation of MXenes technique may be useful in the development of high-rate anode materials for electrochemical energy storage.

2.4. Other fluorine-free etching method

In addition to the Lewis acid molten salt method, there are many other fluorine-free etching methods, such as alkali etching, halogen etching, hydrochloric acid, hydrothermal etching, which all indicate that the development of MXene etching is moving towards low concentration, no fluoride, adjustable and diversified development.

In 2018, MAX was etched for the first time using high-concentration sodium hydroxide (NaOH) etching conditions, and the etched MXene had an accordion-like structure [76]. This method marked the first discovery of fluorine-free surface group MXene. This synthetic route was inspired by the Bayer process widely used in bauxite refining. The synthesis process yields multilayer $Ti_3C_2T_x$ with a purity of about 92 wt% and is completely free of fluorine. The obtained $Ti_3C_2T_x$ thin film electrode thickness is only about 52 μm.

Wang *et al.* attempted directly utilizing hydrochloric acid to etch the MAX phase fluoride-free Mo_2C MXenes with excellent efficiency [77]. Because of the surface functional groups formed by the HCl etch process, the Mo_2C electrodes produced by this technique display exceptional electrochemical performance in supercapacitors and sodium-ion batteries. Fig. 5c depicts the schematic process. This research should offer a lot of promise for the diversification of MAX and MXenes analogues, as well as the activation/stabilization of perfect surfaces for a wide range of applications.

Halogen etching is an innovative etching technique that enables control over the surface functional groups of MXene [78]. A room-temperature etching approach utilizing halogens (Br_2, I_2, ICl and IBr) in anhydrous solutions is suggested for the production of MXenes from Ti_3AlC_2 [78]. The radical-mediated process is very sensitive to the molar ratio of halogen to MAX phase, halogen concentration, solvent, and temperature. Fig. 5d depicts the formation process in general terms. The versatility provided by solvent-based halogen etching will enable a broad variety of intriguing applications.

Up to now, almost all discovered MXenes were synthesized by selective etching *via* one of the aforementioned methods in laboratory. However, when it comes to the industrialization of MXene, more factors have to be considered. For instance, the surface groups and flake size are related to the properties of MXene [79]. Therefore, scale-up and high-yield synthesis of MXene without change of these characteristics is essential. To realize the wide use of MXene, the long-term thermal stability under ambient environment must be enhanced. Various strategies have been devel-

oped to overcome this problem, such as surface modifying, hydrogen annealing and capping the edges of MXene by polyanions [80–82]. However, the practical application feasibility of these methods remains to be verified. In addition, considering the practical complex multicomponent systems, further basic research on the multifunctionality of MXene should be conducted.

3. MXene-based gas sensors

MXenes have high electrical conductivity and an abundance of functional groups, and their huge specific surface area provides an abundance of active sites, making them popular in gas sensing. The large specific surface area of MXenes promotes gas molecule diffusion and interaction with gas-sensing materials and gas molecules. Charge transfer happens at the surface of the MXene layered structure when gas molecules are exposed to it, resulting in a tuning of the total conductivity of the sensing layer. In general, oxidizing gas take electrons from MXene nanomaterials, whereas the majority of volatile organic compounds (VOCs) provide electrons to MXene nanomaterials. Furthermore, MXenes and their composites are also promising room-temperature gas-sensing materials due to the high sensitivity gas response. The carrier concentration and mobility are directly related to the conductivity of semiconductor materials. Higher conductivity will lead to higher carrier concentration and movement speed. Temperature and conductivity are also highly correlated. Metal oxide semiconductors require higher operating temperatures because, within a certain range, the conductivity of semiconductors increases with temperature. MXene has a high carrier mobility, good metal conductivity, and a maximum known conductivity of up to 20,000 S/cm, which can offers an effective transport channel for electronic charges when combined with the distinct layered morphology [83]. In addition, MXene possesses the characteristics of rapid charge transfer, abundant surface functional groups, a sizable specific surface area, high porosity, and a wealth of active sites for gas adsorption. Therefore, at room temperature, MXene can quickly adsorb gas molecules from the environment to realize the function of gas response. Gas sensors made of MXenes and their composites have demonstrated excellent gas response at room temperature such as $Ti_3C_2T_x$, Mo_2CT_x, Co_3O_4@PEI/$Ti_3C_2T_x$ and $Ti_3C_2T_x$/ZnO [84–91].

Results from prior investigations have shown that the effective methods for enhancing gas sensing capabilities of MXenes include partial oxidation, metal ion intercalation, and sulfur doping. MXene and other materials formed compounds with significantly improved gas-sensing properties over the original materials. Thus, many researchers focus on the gas-sensing properties of MXene-based compounds, with the goal of developing better gas-sensing enhancement strategies.

3.1. Pristine MXenes gas sensor

3.1.1. Ti_2CT_x MXene gas sensor

As one of the thinnest MXenes, Ti_2C is a potential gas sensing material. Researchers conducted both theoretical and experimental studies to investigate the gas sensing properties of Ti_2C. The functional group, such as Ti_2CO_2 with its semiconductor properties, Ti_2C, Ti_2CF_2, and $Ti_2C(OH)_2$ with its metallic properties, greatly influences the electrical property of MXene [92,93]. Considering its semiconducting properties, there may be more possible uses for Ti_2C with oxygen termination than for other terminations. To explore its possible uses as a gas sensor, Yu *et al.* provide a research regarding the adsorption of CH_4, NH_3, H_2, CO, O_2, CO_2, N_2, and NO on single layer Ti_2CO_2 [94]. Only NH_3 could be chemisorbed on Ti_2CO_2, indicating that Ti_2CO_2 MXene might be a potential option for an NH_3 sensor with excellent selectivity and sensitivity. In terms of experimental research, Ti_2CT_x MXene was prepared from the Ti_2AlC MAX phase powder by selectively etching off the Al layers after the HCl and LiF etching treatment [95]. Then it was incorporated into a visible-light-enhanced CH_4 sensor. The response/recovery time were also significantly shortened in the Ti_2CT_x MXene-based sensor, which demonstrated a more than seven-fold increase in CH_4 sensing performance under visible-light irradiation.

3.1.2. $Ti_3C_2T_x$ MXene gas sensor

$Ti_3C_2T_x$ MXene has been prepared in experiments as early as 2011. Due to the unique properties of MXene, after more than ten years of development, it has been currently used in heavy metal ion adsorption, electromagnetic shielding catalysis, piezoelectric, biological sensing, *etc.* In the future, there is great potential for large-scale applications in electrochemical energy storage, supercapacitors, *etc.* Sensors are not among the first predicted application areas, especially gas sensors. Up till 2017, Lee *et al.* created a $Ti_3C_2T_x$ nanosheet-based room temperature gas sensor [96]. The $Ti_3C_2T_x$ sensors successfully measured ethanol, methanol, acetone, and ammonia gas at room temperature and showed a p-type sensing behavior. A possible sensing mechanism of the sensor is also proposed in terms of the transfer of majority charge carriers through the interaction between the sensing substance and the sensing material (Fig. 6a). Two alternative reactions may be used to resolve the electron transmission from the $Ti_3C_2T_x$ film to Ammonia gas, depending on the kind of surface termination.

$$2NH_3 + 3O^- \rightarrow N_2 + 3H_2O + 3e^- \quad (4)$$

$$NH_3 + OH^- \rightarrow NH_2 + H_2O + e^- \quad (5)$$

NH_3 gas molecules can be adsorbed on the surface functional groups such as O^- and OH^- of $Ti_3C_2T_x$. Therefore, electrons will be generated through Eqs. 4 and 5, resulting in hole-electron recombination and subsequent increase in resistance.

Early illness detection requires the identification of VOCs at sub-parts per million (ppm) levels in exhaled breath. Low electrical noise and high signal are two indispensable conditions for high sensitivity, induced by high conductivity and abundant adsorption sites respectively. Traditional gas-sensing materials cannot meet these two requirements. According to research by Kim *et al.*, two dimensional metallic carbide MXenes exhibit higher metallic conductivity, less noise, and completely functionalized surfaces than conventional semiconductor channel materials [97]. Fig. 6b(i) displays the gas response of MoS_2, BP, rGO, and $Ti_3C_2T_x$ sensors when exposed to 100 ppm of acetone, ethanol, and ammonia in real time. The graph shows the highest response of each sensor to the different gases utilized. The Signal-Noise-Ratio values of the MoS_2, BP, rGO, and $Ti_3C_2T_x$ sensors are compared in Fig. 6b(ii) for 100 ppm acetone, ethanol, ammonia, and propanal. For ammonia, the SNR value of $Ti_3C_2T_x$ was 160, which was about 3.8 times more than that of BP.

The gas-sensing properties of pure MXene materials are closely related to the precursor carbon sources, atom defects and the lateral dimension of the flakes. In order to produce MXene gas sensors, Shuck *et al.* synthesized Ti_3AlC_2 from titanium carbide, carbon lampblack, and graphite (Fig. 6c) [98]. The three MAX phase-converted MXenes show different morphologies and properties. The responsiveness of the sensors to three VOCs (ethanol, acetone and ammonia) was tested. The results show that MXene films produced by titanium carbide have the highest response, followed by graphitic carbon sources, with materials from carbon soot having the lowest sensitivity. At the same time, MXene with titanium carbide as carbon source shows good selectivity to ammonia. The atom defects have a major impact on adsorption and electronic

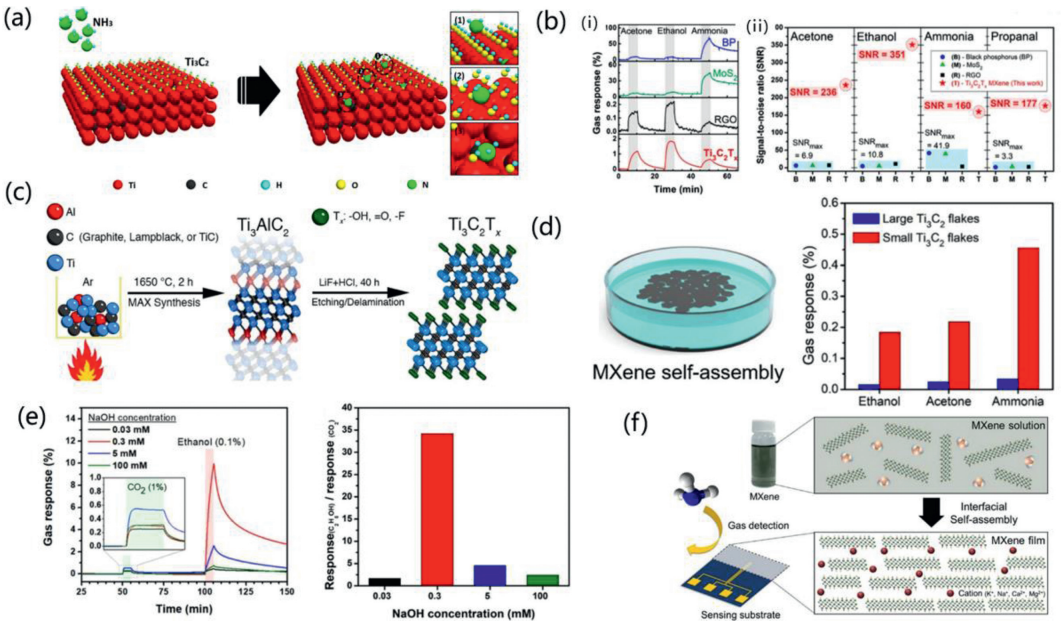

Fig. 6. (a) Schematic illustration of the possible gas-sensing mechanisms of $Ti_3C_2T_x$ for NH_3 gas. Reprinted with permission [96]. Copyright 2017, American Chemical Society. (b) (i) Real-time gas response behavior of BP, MoS_2, RGO, and $Ti_3C_2T_x$ sensors and (ii) maximal SNR values of sensors. Reprinted with permission [97]. Copyright 2018, American Chemical Society. (c) Synthesis of Ti_3AlC_2 from different carbon sources followed by $Ti_3C_2T_x$ synthesis. Reprinted with permission [98]. Copyright 2019, American Chemical Society. (d) Fabricated ultrathin MXene films and gas responses as a function of detected gas for each film. Reprinted with permission [100]. Copyright 2019, American Chemical Society. (e) Gas sensing performance of NaOH-treated $Ti_3C_2T_x$ sensors at room temperature. Reprinted with permission [101]. Copyright 2019, American Chemical Society. (f) Synthesis schematic of MXene transparent thin films. Reprinted with permission [71]. Copyright 2021, American Chemical Society.

properties of MXene, which is vital for its gas sensing performance. Lu *et al.* fabricated oxidized $Ti_3C_2T_x$ crumpled spheres with numerous Ti atom defects by ultrasonic spray pyrolysis technology [99]. The results showed that the adsorption energy of $Ti_3C_2T_x$ with a Ti-O vacancy to gas molecules was greatly reduced, and the charge transfer was more obvious, which proved that the sensing ability of $Ti_3C_2T_x$ with Ti atom defect to gas was significantly enhanced. The smaller lateral size and larger defect concentration mean that the flakes have more active edges and reaction sites. This will boost the material's ability to detect gases by promoting the adsorption of gas molecules to it. According to research, mechanical vibration or sonication would reduce the size of MXene and add more defects. Using an composite interfacial assembly method, Kim *et al.* fabricated a thin $Ti_3C_2T_x$ film capable of 320 signal-to-noise ratio [100]. The film assembled from small MXene flakes had a gas response 10 times that of the film assembled from large flakes. Films morphology and gas-sensing properties is shown in Fig. 6d.

The preparation technology of single-layer MXene is not yet mature. At present, most MXene materials are mostly few-layer materials with less than or equal to 5 layers and multi-layer materials with more than 5 layers. Interlayer spacing also significantly affects gas sensing performance. Using *in-situ* XRD measurements, Koh *et al.* studied the interlayer spacing change of $Ti_3C_2T_x$-MXene following gas introduction [101]. The findings reveal that the concentration of intercalated sodium ions is critical for controlling the swelling behavior and gas-sensing characteristics. The degree of swelling was in excellent accord with the strength of the gas response, and the $Ti_3C_2T_x$ sensing channel treated with 0.3 mmol/L NaOH obtained the maximum gas selectivity to ethanol vapor, as shown in Fig. 6e. This finding suggests that adjusting the interlayer spacing of $Ti_3C_2T_x$ is critical for improving gas sensing characteristics. The interlayer spacing of MXenes can be adjusted by intercalation of different ions, molecules and ionic liquid. For instance, Liang *et al.* synthesized MXene with different interlayer spacings by intercalation of alkylammonium cations [102]. Chen *et al.* reported the interlayer spacing of MXene was increased from 1.23 nm to 1.40 nm by intercalation of 1,4-butanediamine. Self-assembly had been used by Kim *et al.* to create metal ion-intercalated $Ti_3C_2T_x$-MXene films (Fig. 6f) [71]. The metal ion-intercalated MXene films exhibited stronger gas sensitivity than the pristine MXene films, which had a 10-fold higher signal-to-noise ratio when the films were utilized as NH_3 gas sensor. The above studies all show that metal ion intercalation has a positive effect on the gas sensing properties of pristine MXene materials, which provides ideas for subsequent research.

3.1.3. Other MXene gas sensors

Carbon-based titanium compounds (Ti_2CT_x and $Ti_3C_2T_x$ MXene) gas sensors are most widely explored among all discovered MXene family [103]. However, a few gas sensors have been reported based on other MXenes, such as V_2CT_x, $V_4C_3T_x$ and Mo_2CT_x. For instance, the monitoring of flammable and explosive gases is the top priority of industrial safety production, and effective monitoring can avoid significant loss of personnel and property. Hydrogen and methane are typical non-polar gases with weak adsorption properties, which are difficult to identify and trace at room temperature by traditional gas-sensing materials. By using selective etching and intercalation, single-layer and multiple-layer V_2CT_x flakes were made [104]. These flakes were then drop onto a polyimide platform to make gas sensors. The results of the gas-sensing tests indicate that the 2D V_2CT_x gas sensor is capable of detecting polar and non-polar gases at ambient temperature. The detection limits for hydrogen and methane, respectively, are 2 ppm and 25 ppm, respectively. It has made a breakthrough in the monitoring of non-polar gases, which exceeds other 2D materials previously reported.

As a non-invasive medical diagnostic method, signature exhaled breath detection has become increasingly popular. For example, the exhaled marker of diabetes is acetone, and developing a gas sensor that can detect low concentrations of acetone can help in the clinical diagnosis of diabetes. Emerging MXene $V_4C_3T_x$ was pro-

duced by selective etching of V_4AlC_3 at room temperature, and its potential as an acetone sensor was investigated [90] . The findings demonstrate that $V_4C_3T_x$ has strong acetone sensing capability, with a detection limit of 1 ppm at ambient temperature, which is lower than the 1.8 ppm diagnostic threshold for diabetes. In addition, the breath exhaled by the human body contains a lot of water vapor, which will affect the detection results of the gas sensor. The $V_4C_3T_x$-prepared sensor demonstrates good selectivity for acetone in acetone-and-water-vapor-combined gases. and is a promising acetone gas-sensing material, which is expected to be applied in the actual diagnosis of diabetes.

Toluene has been regarded as one of the most hazardous VOC pollutants in air and the trace detection of toluene was important implications for improved healthcare. Mo_2CT_x exhibiting superior electronic conductivity and chemical activity, shows promising potential in trace gas detection. Delaminated Mo_2CT_x was prepared by selective etching of Mo_2Ga_2C precursor and evaluated as the sensing material for toluene sensor [105]. The results showed that toluene sensor had a low detection limit of 220 ppb and a sensitivity of 0.0366 Ω/ppm at a toluene concentration of 140 ppm, which exhibited an excellent selectivity toward toluene against the other VOCs.

In addition, the theoretical simulations were also carried out on the gas sensing performance of some MXenes. For instance, Hu *et al.* systematically simulated the adsorption of 17 kinds of gases (including NH_3, NO_x, CO_x and SO_x) on the single-layer M_2CS_2 (M = Sc or Y) based on the first principle theory [106]. The simulation results show that Sc_2CS_2 has high sensitivity and good selectivity to NO, nicotine and ethanol. Compared with M_2CS_2, Y_2CS_2 has higher chemical reactivity and shows high sensitivity and selectivity to NO. At the same time, the recovery time of M_2CS_2 is very short, and it can be reused, indicating that this material has good cycle stability. Naqvi *et al.* conducted spin-polarized DFT calculations with vdW correction to investigate the sensing propensity of various gases, such as CH_4, CO on M_2NS_2 (M = Ti, V) sheets [107]. The results revealed that Ti_2NS_2 and V_2NS_2 sheets possessed similar gas-sensitive properties and can be utilized as a gas sensing material for NO, NO_2, H_2S and SO_2.

3.2. MXenes composite gas sensor

The ability of pristine MXene to detect gases is mostly influenced by their own structure and physical characteristics. The improvement of gas sensing performance by changing the carbon source of the MAX phase precursor, reducing the lateral size of the flakes, and increasing the defect concentration is very limited. Synthesis of MXene composites proves to be an effectively approach to drastically improve performance. Since MXenes show a higher specific surface area than bulk materials due to their special layered structure, the multitudinous active sites on are exposed and enable sufficient surface reactions. For instance, various inorganic and organic species, such as metal oxide semiconductors, transition metal dichalcogenides (TMDs), graphene and organic polymers, can bind to the surface of MXenes, which improve their complexity and functionality. Among them, metal oxides mainly include SnO_2, TiO_2, ZnO, α-Fe_2O_3, WO_3, In_2O_3 and CuO. These active metal oxides have already shown excellent gas sensing properties when they are applied to gas sensors. Consequently, integrating them with MXene may enhance the gas-sensing capabilities of MXene materials.

3.2.1. MXene/TMDs

Two-dimensional TMDs have shown excellent electronic, magnetic, optical, mechanical, catalytic and sensing properties, of which MoS_2 is the most widely used [108–110]. MoS_2 powder was combined with Ti_3C_2 MXene to produce Ti_3C_2-MoS_2 composites. These composites had excellent metallic conductivity and a surface that was functionalized (Fig. 7a) [111]. The composite material offers a promising notion for the detection of hazardous gases at room temperature due to its ability to detect not only low-concentration NO_2 but also toxic gases like methane and ammonia. Also as a NO_2 sensor, WS_2 is also an promising candidate material. Xia *et al.* prepared a $Ti_3C_2T_x/WS_2$ hybrid film for room temperature radio and television NO_2 sensors [112]. The test results show that the $Ti_3C_2T_x/WS_2$ gas sensor has good NO_2 selectivity, high response/recovery rate, good stability and low detection limit. Composites made of MXenes and TMDs also have a position in the de-

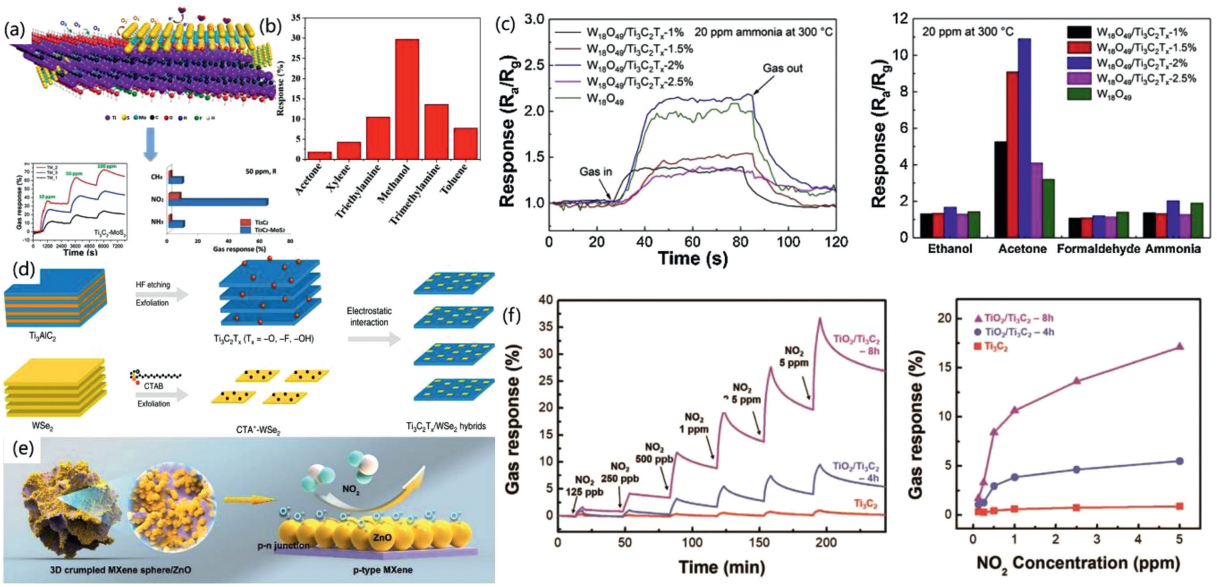

Fig. 7. (a) The NO_2-sensing mechanism of Ti_3C_2-MoS_2. Reprinted with permission [111]. Copyright year 2021, Elsevier Ltd. (b) Selectivity curves of $In_2O_3/Ti_3C_2T_x$. Reprinted with permission [114]. Copyright year 2021, Elsevier Ltd. and Techna Group S.r.l. (c) Response-recovery curves and comparison with different sensors. Reprinted with permission [116]. Copyright year 2019, Elsevier B.V. (d) Schematic illustration of $Ti_3C_2T_x/WSe_2$. Reprinted with permission [113]. Copyright 2020, Springer Nature. (e) The sensing characteristic of MXene sphere and MXene sphere/ZnO. Reprinted with permission [91]. Copyright 2020, Elsevier B.V. (f) Gas sensitivity performance of TiO_2/Ti_3C_2. Reprinted with permission [117]. Copyright 2020, Wiley-VCH GmbH.

tection of VOCs. A straightforward surface modification and exfoliation procedure was used to create the $Ti_3C_2T_x/WSe_2$ nanohybrid (Fig. 7d) [113]. Compared with the sensors made of pure $Ti_3C_2T_x$ and pure WSe_2, the $Ti_3C_2T_x/WSe_2$ hybrid sensor was 12 times more sensitive to ethanol, and the gas sensing performance was greatly improved.

As can be seen from the above discussions, the MXene composites hybridized with TMD overcome the instability and oxidation tendency of a single MXene, thereby providing a novel way of practical implementation of MXene materials. This opens the door to new possibilities for the use of MXene materials.

3.2.2. MXene/MOS

A vast number of publications have described resistive gas sensors based on metal oxide semiconductors (MOS). It has emerged as the most promising candidate material in the area of gas sensors due to its cheap cost, ease of production, high stability, and response to many gases. MOS is classified into two types based on carrier differences: n-type and p-type. n-type employs negatively charged electrons as carriers, while p-type uses positively charged holes as carriers. ZnO, SnO_2, Fe_2O_3, In_2O_3 and WO_3 are common n-types, whereas CuO, Co_3O_4, and NiO are common p-types. Indium oxide is a novel n-type transparent semiconductor functional material with a large band gap, low resistivity, and strong catalytic activity that has found widespread use in optoelectronics, gas sensors, and catalysts. In_2O_3 nanocubes/$Ti_3C_2T_x$-MXene nanocomposites were created by Liu *et al. via* a straightforward hydrothermal self-assembly process [114]. The findings of the characterization indicated that the surface In_2O_3 nanocubes are well disseminated on the surface of the layered $Ti_3C_2T_x$-MXene and form a heterojunction structure. This contributes to an improvement in the material's gas sensing ability. And the composite material has a high response and high selectivity to methanol (Fig. 7b), making it a suitable material for detecting methanol gas at room temperature because of these characteristics. While this is happening, the detection limit may be lowered to the ppm level, and the time it takes to respond and recover can be cut down to 6.5 s and 3.5 s, respectively. Xu *et al.* also reported the sensing performance of MXene/SnO_2 to ethanol, which was twice that of the pristine SnO_2 sensor [115]. The combination of layered MXenes with metal oxide semiconductors presents a fresh opportunity for the creation of gas sensors that operate at room temperature in the future.

Conventional acid solution etching of $Ti_3C_2T_x$ nanosheets results in easy stacking and loss of high specific surface area, limiting their gas sensing capabilities. To solve this problem, Yang *et al.* prepared 3D wrinkled MXene $Ti_3C_2T_x$ spheres and sphere/ZnO samples by ultrasonic spray pyrolysis [91]. This method not only maintained the original MXene's high specific surface area but also brought in plenty of active edges from the wrinkle. The structure and adsorption demonstration of NO_2 gas molecules are shown in Fig. 7e.

The oxygen vacancy-rich non-stoichiometric phases of tungsten oxides (WO_x, $x \leq 3$) make them excellent candidates for use as gas sensing materials because they offer more active edges for gas adsorption. Based on this theory, Sun *et al.* produced $W_{18}O_{49}/Ti_3C_2T_x$ composites using a straightforward thermal solvent technique [116]. The gas detecting test results demonstrated the sensor's low detection limit for acetone, high responsiveness, strong selectivity, long-term oxidative stability, and quick response/recovery rate. Under the operating temperature of 300 degrees and the concentration of the gas to be tested at 20 ppm, the sensitivity defined as the resistances of the sensors in the air to that in the target gas (R_a/R_g) can reach 11.2, which is better than the original $Ti_3C_2T_x$ and $W_{18}O_{49}$ materials (Fig. 7c).

Ti_3C_2 has low thermal stability and is easily oxidized to TiO_2 at high temperature, which limits some of its development. However, we can also use this feature to generate TiO_2 on the surface of Ti_3C_2 *in situ* and form a Schottky barrier with Ti_3C_2 to improve the performance of the material. Fig. 7f shows the influence of Schottky barrier on the gas-sensing performance. Because of this character, we can use some special properties or apparent shortcomings of materials to expand the research direction, and provide novel ideas for our future scientific research work. Both Choi *et al.* and Liu *et al.* used a basic hydrothermal technique to fabricate TiO_2/Ti_3C_2 composite gas sensor [117,118]. In comparison to the original Ti_3C_2 MXene, the sensitivity to NO_2 has been enhanced by a factor of ten, reaching the lower detection limit of ppb level, which offers a more reliable method for detecting NO_2 gas.

3.2.3. MXene/rGO

In the realm of two-dimensional material gas sensors, graphene has a significant place because to its ultra-high electrical conductivity as well as its vast specific surface area. Graphene is a typical two-dimensional material. A shining example of this is the mixing of materials that are just two-dimensional. When graphene is coupled with MXene, it will exhibit unique physical and chemical characteristics. This has the effect of increasing the gas-sensing capabilities of MXene, which is a win-win situation for everyone involved. Flexible wearable sensing materials have broad application prospects and are also an important research direction that cannot be ignored in gas sensing, especially in early medical diagnosis. Graphene has high mechanical flexibility and weavability and is manufactured as a hybrid fiber gas sensing material with $Ti_3C_2T_x$ MXene by a wet spinning fiber technique [84]. In the bending test, the hybrid fibers demonstrated outstanding mechanical flexibility and low noise resistance (Fig. 8a(i)), indicating their significant potential for use in wearable devices. As demonstrated in Figs. 8a(ii) and (iii), the hybrid fibers have greatly better ammonia sensing capability, longer bending cycles, and other good features. A lab coat was also made by the conventional weaving method, and the material's gas-sensing characteristics were preserved, which is a reliable flexible, portable and wearable gas-sensing material. Tran *et al.* prepared rGO/$Ti_3C_2T_x$ composites with large specific surface area by a simple ultrasonic method (Fig. 8b) [119]. The heterojunction structure not only shows a large response to NO_2 gas, but also shows a response performance to toxic gases such as CH_4, which provides a research idea for the monitoring of toxic gases at room temperature. Similar to graphene, one-dimensional carbon nanotubes (CNTs) also have some special physic properties, such as large specific surface area, abundant adsorption sites and high electrical conductivity. When evaluated as a sensing material for gas sensing, CNTs demonstrate p-type properties and target gas molecules could be absorbed by van der Waals forces [120]. However, few research on the gas sensing properties of MXene/CNTs was reported.

3.2.4. MXene/polymer

Due to their great sensitivity and cheap cost, polymers are also widely utilized in MXene-based gas-sensing composites. PAM, PANI, PPy, PEDOT:PSS, PEI, *etc.*, are the most widely used polymers [121–126]. A very interesting phenomenon is that the composites formed by MXene and conductive polymers all perform well in ammonia gas sensing.

Zhao *et al.* produced a nanocomposite that could be used at room temperature and was composed of $Ti_3C_2T_x$ MXenes material and cationic polyacrylamide (CPAM) [121]. A stage in the manufacturing process of CPAM/$Ti_3C_2T_x$ nano-composites is shown in Fig. 8c. When utilized in an NH_3 gas sensor, the composite material demonstrates outstanding stability, with a response of 4.7% to 200 ppm ammonia gas as well as a quick response/recovery rate.

Wang *et al.* developed a polyaniline/Nb_2CT_x ammonia gas sensor with rich three-dimensional structure, which can realize sen-

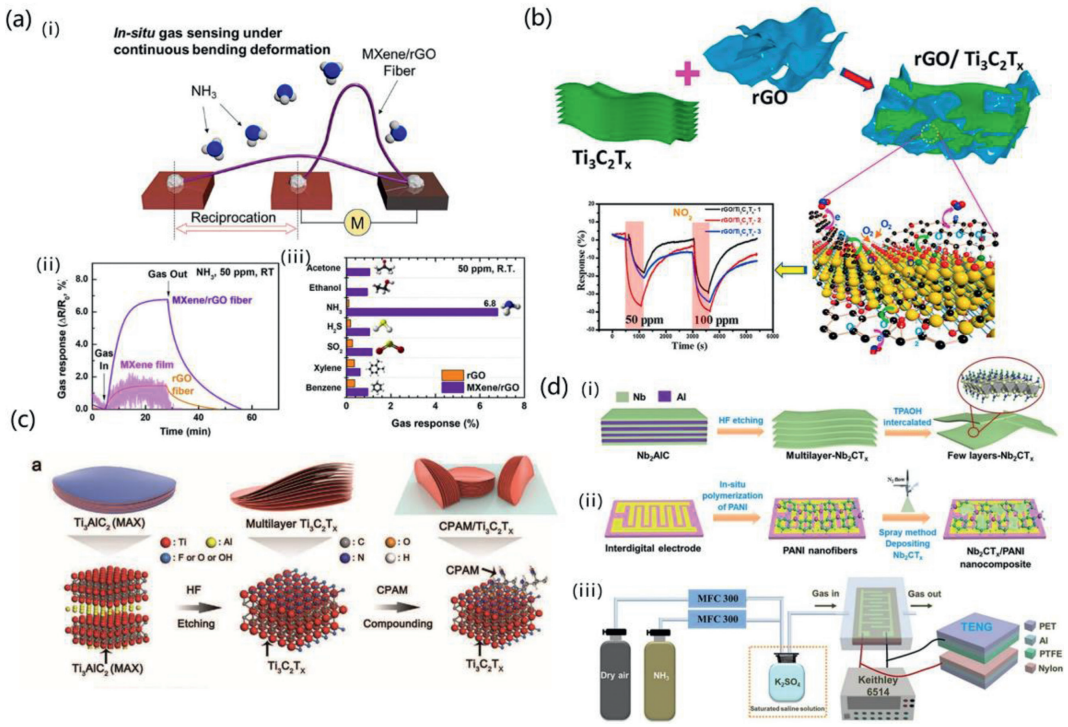

Fig. 8. (a) (i) Schematic illustration of the fiber bending test, comparison of (ii) the gas response and gas selectivity of MXene film, (iii) comparison of the gas selectivity. Reprinted with permission [84]. Copyright 2020, American Chemical Society. (b) Schematic synthesis process, NO_2-sensing mechanism and performance of rGO/$Ti_3C_2T_x$ heterostructures. Reprinted with permission [119]. Copyright 2021, Elsevier B.V. (c) Schematic illustration of fabrication and gas-sensing principle of CPAM/$Ti_3C_2T_x$ nanocomposites. Reprinted with permission [121]. Copyright 2020, Wiley-VCH Verlag GmbH & Co. KGaA, Weinheim. (d) Synthesis process of (i) ultrathin 2D Nb_2CT_x nanosheets and (ii) Nb_2CT_x/PANI sensor, and (iii) schematic diagram of the TENG-driven gas sensing system. Reprinted with permission [123]. Copyright 2020, Elsevier B.V.

sitive ammonia gas detection in humid environment [123]. Fig. 8d depicts both the synthesis process as well as the gas sensing procedure. In the case of relative humidity of 62.0%, the response to 50 ppm ammonia gas is as high as 205.39%, far exceeding the previously reported gas-sensing materials. It is an MXene-based gas-sensing material with ultra-high sensitivity. The high responsiveness was maintained even at 87.1% relative humidity, which was attributed to the hydrogen bonding formed between PANI and Nb_2CT_x. This kind of gas-sensing material with anti-humidity properties has great application value in the diagnosis of human exhaled gas and gas sensing applications related to the marine environment. In terms of agricultural ammonia detection, Li *et al.* synthesized polyaniline (PANI)/$Ti_3C_2T_x$ hybrid sensitive film and verified the feasibility of this material in the detection of ammonia volatilization through agricultural simulation experiments [127]. The results show that the material can exhibit good NH_3 sensing performance at room temperature (10–40 °C) and a broad range of relative humidities (20%-80%).

Jin *et al.* successfully prepared novel PEDOT:PSS/$Ti_3C_2T_x$ composites by *in-situ* polymerization [125]. Fig. 9a shows a diagrammatic representation of the synthesis of PEDOT:PSS/MXene composites as well as the construction process of a composite-based gas sensor. In reaction to 100 ppm of NH_3, the composites exhibited a high response of 36.6%, which may be attributed to the synergistic impact of the PEDOT:PSS polymer and the $Ti_3C_2T_x$-MXene 2D materials. Because of the huge number of reaction sites in the $Ti_3C_2T_x$ MXene layer and the direct charge transfer between PEDOT:PSS and $Ti_3C_2T_x$ MXene, the good performance may be due to these factors.

3.2.5. MXene-based multicomponent composites

Combining MXenes with MOS is a potential approach for enhancing room-temperature gas sensing capabilities. However, few investigations on MXene and MOS composites are available. Through a combination of solution mixing and oxidation treatment, Wu *et al.* successfully obtained a SnO_2-TiO_2-$Ti_3C_2T_x$ sensor for gas detection at room temperature [128]. SnO_2-TiO_2-$Ti_3C_2T_x$ hybrid film was shown in Fig. 9b(i). At a temperature of 25 degrees Celsius, the sensor demonstrates good sensitivity, a low limit of detection, outstanding selectivity, and long-term stability for NO_2 measurements, shown in Fig. 9b(ii). The synergistic effect of the three phases is essential for the marked improvement in NO_2 sensing provided by the SnO_2-TiO_2-$Ti_3C_2T_x$ sensor when compared with the SnO_2, $Ti_3C_2T_x$, and TiO_2-$Ti_3C_2T_x$ sensors, respectively.

Through a straightforward and productive hydrothermal treatment, Liu *et al.* were able to effectively build a three-dimensional $Ti_3C_2T_x$/rGO/CuO aerogel (Fig. 9c) [129]. At room temperature, the aerogel sensor is capable of displaying excellent sensitivity to very low quantities of volatile organic compounds (VOCs). The 3D MXene/rGO/CuO aerogel has a high response reach to 50.09% at 100 ppm, rapid reaction and recovery speed (6.5 and 7.5 s, respectively), and excellent selectivity to acetone gas. It has been shown that the three-dimensional combination of MXene also has excellent gas sensing characteristics.

Ranjbar *et al.* designed a Schottky structure synthesized from $Ti_3C_2T_x$ MXene sheets with chrysanthemum-like V_2O_5/$CuWO_4$ [130]. MXene/V_2O_5/$CuWO_4$-based sensors were exposed to various analyte gas molecules. The comparison at the same concentration shows that the fabricated sensor has excellent selectivity and ultra-high sensitivity to ammonia. The findings provide evidence that the sensor has excellent characteristics, including high sensitivity, an incredibly fast reaction time, strong selectivity, repeatability, long-term stability, and a low working temperature. Fig. 9d presents a possible mechanism for the ammonia detection process. Due to the very high work function of the MXene, a Schottky barrier is formed once the metallic $Ti_3C_2T_x$ MXene comes in contact

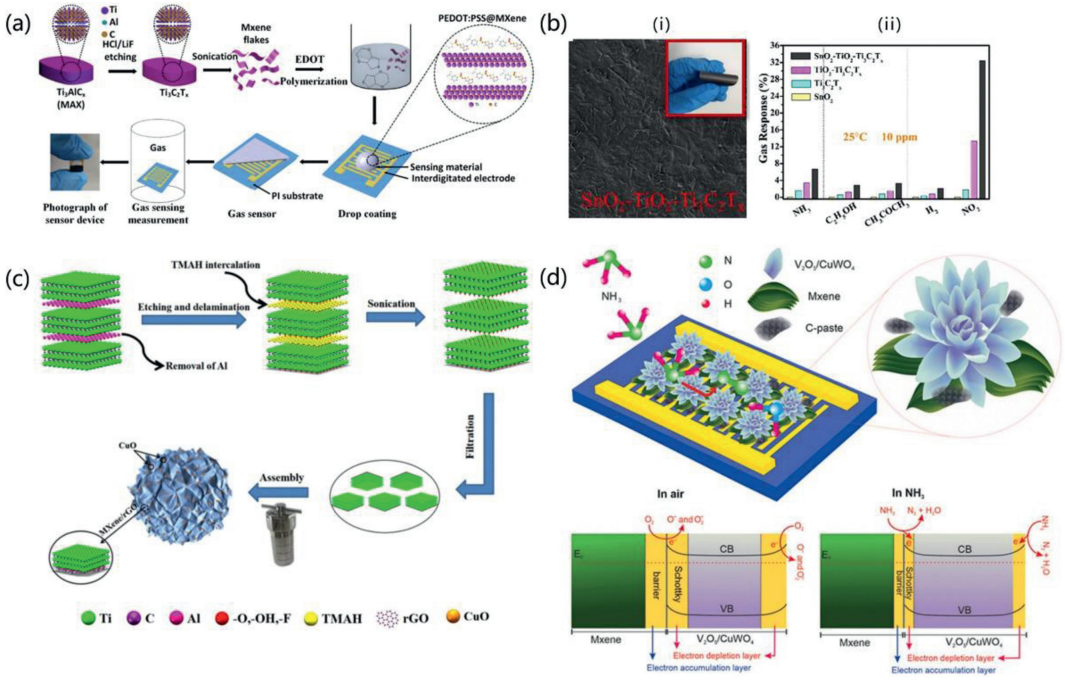

Fig. 9. (a) Schematic illustration for the synthesis of PEDOT:PSS/MXene composites and the corresponding gas sensor. Reprinted with permission [125]. Copyright 2020, American Chemical Society. (b) (i) SnO_2-TiO_2-$Ti_3C_2T_x$ hybrid film, (ii) gas sensing mechanism and (iii) gas sensing performance. Reprinted with permission [128]. Copyright 2021, Elsevier B.V. (c) Schematic illustration of 3D MXene/rGO/CuO aerogel synthesized process. Reprinted with permission [129]. Copyright 2021, Elsevier B.V. (d) Mechanism of ammonia sensing by $Ti_3C_2T_x/V_2O_5/CuWO_4$ sensor. Reprinted with permission [130]. Copyright 2021, Elsevier B.V.

with $V_2O_5/CuWO_4$ in the air. Then, surface adsorbed oxygen would capture some electrons from the n-type $V_2O_5/CuWO_4$ heterostructure to generate negatively charged oxygen molecules adsorbed at its surface, resulting in the formation of a depletion layer of a certain thickness on the V_2O_5 surface. When exposed to ammonia, ammonia reacts with negative oxygen ions to form nitrogen and water, the electrons trapped by O^- and O^{2-} would go back to the $V_2O_5/CuWO_4$ surface or its junction with MXene, causing a considerable reduction in resistance.

3.3. Sensing mechanism

Gas sensors are used to detect the category, concentration and composition of target gases, and convert them to electrical signals. The basic sensing mechanism is that the resistance of pure MXenes and MXene-based composites changed after gas adsorption due to electron-donating/accepting from target gases. The MXene was supposed to possess the characteristics of p-type semiconductor at first [131]. On the basis of this mechanism, when MXene is exposed to reducing gas (acetone, ethanol, methanol and ammonia), reducing molecule are absorbed on the surface of MXene and ionized by electron-donating. Thus, the number of majority charge carriers of MXene decreases which results in the increase of the resistance after reducing gas adsorption and decreases after the gas desorption. Following this mechanism, the resistance of MXene should decrease when exposed to oxidizing gas because of electron-accepting. However, the subsequent experimental results show that the resistance of MXene always increase when exposed to all the gas, regardless of the type of gases [97] . To explain this phenomenon, many other different mechanisms were proposed: (1) The universal increase of the resistance was due to its metallic conductivity, where gas adsorption reduces the number of carriers and increases the channel resistance [97]. (2) The interlayer swelled after gas adsorption, which hinders the out-of-plane electron transport and increase electrical resistance [101]. (3) The adsorption of gas on the MXene surface increase the electron and decrease the conductivity of the MXene [132]. Even though those mechanisms could explain the increase resistance of MXene when exposed to all the gas, the exact gas-sensing mechanism of MXene is still not completely.

The sensing mechanism of MXene composite mainly depends on the nature of its component materials and the interfacial interactions (such as Schottky junctions) between them. As for MXene/MOS, metal oxides, an important component of the composite, are divided into p-type and n-type semiconductors [133]. The resistance changes of metal oxides are related to the type of semiconductors and target gases (oxidizing or reducing). For p-type semiconductors, such as NiO and CuO, oxidizing gases (electron-acceptor) decrease the resistance of semiconductors, while reducing gases increase the resistance of semiconductors [134]. For n-type semiconductors, such as SnO_2 and ZnO, oxidizing gases (electron-acceptor) decrease the resistance of semiconductors, while reducing gases increase the resistance of semiconductors [135]. Atomic vacancies, typically oxygen vacancies, are often constructed in metal oxides, which can provide more free electrons, act as active sites for adsorbing gas molecules and modify baseline resistance [136]. The oxygen vacancies can be constructed by various methods, such as thermal reduction treatment, atomic doping, plasma etching and laser irradiation [137–140]. The thermal reduction treatment is relatively common in many researches, which can adjust the formation of oxygen vacancies and their concentration by controlling the relevant parameters (annealing temperature, annealing time, pressure, and atmosphere). The heterojunction and Schottky junction are often formed at the interface between MXene and metal oxides. For example, the work function of SnO_2 (~4.9 eV) is higher than that of $Ti_3C_2T_x$ MXene (~3.9 eV), therefore, the electrons inject from $Ti_3C_2T_x$ to SnO_2 [141]. Then, an electron depletion layer with a negative zone is formed on SnO_2 side and the positive one is formed on the $Ti_3C_2T_x$ MXene side, which means a built-in electric field created. The built-in electric field counters the transfer of electrons until the Fermi level equilibrates, leading to the formation of a Schottky junction. Thus,

with the addition of MXene in SnO_2, heterostructures are formed, resulting in the creation of Schottky barriers. When MXene/SnO_2 is exposed to oxidizing gas, the electrophilic gas molecules absorb on the surface and capture electrons from the conduction band of the SnO_2. Subsequently, the built-in electric field will be destroyed and more electrons are transferred from MXene to SnO_2, which is contributed to the decrease of resistance. Meanwhile, the Schottky barrier height is also modulated by the surface chemisorbed gases. Generally, MXene, metal oxides and the synergistic enhancement effect (Schottky junctions) between them have combined to change the resistance of MXene/MOS. The gas sensing mechanism of other MXene composite has similar characteristics to that of MXene/MOS. Taking $Ti_3C_2T_x/MoS_2$ for example, 2H-MoS_2 is a ready-state semiconductor material, and Schottky junctions are also formed between composite materials [142]. Similar to that of $Ti_3C_2T_x/SnO_2$, the change of resistance depends on the nature of $Ti_3C_2T_x$, MoS_2 and Schottky junctions between them.

4. Summary and perspectives

This study begins by providing an overview of the many kinds, characteristics, and structures of MXenes. It then moves on to provide an in-depth look at the various ways that may be used to synthesize MXenes. Some of these methods include HF etching, *in-situ* HF synthesis etching, the molten salt approach, the Lewis acid method, and others. Finally, a detailed introduction to the research developments of pure MXene and MXene composites in gas sensing is provided. The gas sensing mechanism is also discussed at the same time. In addition to the classic Ti_3C_2, the original MXene also includes V_2C and V_3C_4, and the composite materials include the composites of MXene and TMDs, MOS, graphene, and conductive polymers. The results show that combining MXene with other materials can significantly improve its gas-sensing performance. Although MXene and its composites have shown promising application potential in gas sensing, many obstacles remain in the way of commercializing MXene gas sensors.

Firstly, since the invention of MXene, the more dangerous HF etching method has been used. Although the subsequent synthesis methods have been continuously improved, other synthesis methods have been discovered one after another, but most of them cannot be popularized. At present, the mainstream method is still HF acid or *in-situ* HF synthesis etching method. This method has a high-risk factor and is inconvenient to operate, and the surface of the generated material contains toxic F functional groups, and cannot be applied to mass production. As a result, there is an immediate need for the development of an MXene synthesis process that is environmentally friendly, non-toxic, and highly effective.

Secondly, the easy oxidation of MXene limits its use to room temperature. Although their antioxidant properties can be enhanced by means of modification, doping, and formation of complexes, long-term signal stability is still not guaranteed.

Thirdly, the gas sensing mechanism of MXenes is more complicated than that of traditional materials such as metal oxides. The pristine MXenes exhibit resistance-increasing behavior to both oxidizing and reducing gases, which is clearly in line with the conventional gas-sensing mechanism of p-type semiconductors. The current sensing mechanism analysis is still in the macroscopic adsorption-swelling model, and further research on the microscopic model is needed.

Finally, humidity is an important environmental factor that need to be considered in practical applications. Typical application scenarios include the detection of disease markers in human exhaled air containing a large amount of water vapor, the detection of polluted gases in the port marine environment, and the detection of harmful gases in agricultural environments with high relative humidity. However, in previous reports, there are few studies using different humidity as an experimental variable. Therefore, in the research process of gas sensors, the actual situation should be fully considered, and objective factors such as humidity and corrosion should be included in the experimental conditions, so that the research results are more convincing.

Declaration of competing interest

The authors declare that they have no known competing financial interests or personal relationships that could have appeared to influence the work reported in this paper.

Acknowledgments

This work was financially supported by the National Natural Science Foundation of China (No. 52172094) and Natural Science Foundation of Shanghai (No. 21ZR1426700).

References

[1] S.S. Wei, Z. Li, A. John, et al., Adv. Funct. Mater. 32 (2021) 2107596.
[2] D.H. Kim, S. Chong, C. Park, et al., Adv. Mater. 34 (2022) 2105869.
[3] M. Kang, I. Cho, J. Park, et al., ACS Sens. 7 (2022) 430–440.
[4] BBC research, https://www.bccresearch.com/partners/verified-market-research/global-gas-sensors-market.html.
[5] M. Khatib, H. Haick, ACS Nano 16 (2022) 7080–7115.
[6] J.M. Suh, W. Sohn, Y.S. Shim, et al., ACS Appl. Mater. Interfaces 10 (2018) 1050–1058.
[7] Y.G. Song, J.Y. Park, J.M. Suh, et al., Chem. Mater. (31) (2018) 207–215.
[8] G.H. Jeong, S.P. Sasikala, T. Yun, et al., Adv. Mater. 32 (2020) 1907006.
[9] G. Lei, H. Pan, H. Mei, et al., Chem. Soc. Rev. 51 (2022) 7260–7280.
[10] J. Liu, L. Zhang, J. Fan, B. Zhu, J. Yu, Sens. Actuator. B: Chem. 331 (2021) 129425.
[11] J. Xuan, L. Wang, Y. Zou, et al., J. Alloys Compd. 922 (2022) 166158.
[12] C. Li, P.G. Choi, K. Kim, Y. Masuda, Sens. Actuator. B: Chem. 367 (2022) 132143.
[13] B. Liu, X. Liu, Z. Yuan, et al., Sens. Actuator. B: Chem. 295 (2019) 86–92.
[14] L. Yang, L. Yang, S. Wu, et al., Sens. Actuator. B: Chem. 323 (2020) 128689.
[15] X. Liu, W. Zheng, R. Kumar, M. Kumar, J. Zhang, Coord. Chem. Rev. 462 (2022) 214517.
[16] F.F. Yin, W.J. Yue, Y. Li, et al., Carbon 180 (2021) 274–297.
[17] G.A. Asres, J.J. Baldoví, A. Dombovari, et al., Nano Res. 11 (2018) 4215–4224.
[18] A. Shahzad, J.M. Oh, M. Azam, et al., Membranes 11 (2021) 605.
[19] C. Tan, X. Cao, X.J. Wu, et al., Chem. Rev. 117 (2017) 6225–6331.
[20] W. Zheng, X. Liu, J. Xie, G. Lu, J. Zhang, Coord. Chem. Rev. 447 (2021) 214151.
[21] X. Wang, W. Liu, C. Wang, et al., Sens. Actuator. B: Chem. 344 (2021) 130190.
[22] X. Wang, W. Liu, T. Wang, et al., Sens. Actuator. B: Chem. 350 (2022) 130876.
[23] Y. Zhao, X. Wang, T. Wang, et al., Appl. Surf. Sci. 604 (2022) 154618.
[24] C. Wang, X. Cheng, X. Zhou, et al., ACS Appl. Mater. Inter. 6 (2014) 12031–12037.
[25] L. Yu, J. Wei, Y. Luo, et al., Sens. Actuator. B: Chem. 204 (2014) 96–101.
[26] B. Behera, S. Chandra, Mater. Sci. Semicond. Process. 86 (2018) 79–84.
[27] P.H. Suman, A.A. Felix, H.L. Tuller, J.A. Varela, M.O. Orlandi, Sens. Actuator. B: Chem. 208 (2015) 122–127.
[28] F.L. Lontio, B. Saruhan, Chemosensors 7 (2019) 42.
[29] W. Yang, L. Feng, S. He, L. Liu, S. Liu, ACS Appl. Mater. Interfaces 10 (2018) 27131–27140.
[30] R. Qin, G. Shan, M. Hu, W. Huang, Mater. Today Phys. 21 (2021) 100527.
[31] B. Anasori, Y. Gogotsi, B. Anasori, Y. Gogotsi, Introduction to 2D transition metal carbides and nitrides (MXenes), 2D Metal Carbides and Nitrides (MXenes): Structure, Properties and Applications, Springer International Publishing, Cham, 2019, pp. 3–12.
[32] A. VahidMohammadi, J. Rosen, Y. Gogotsi, Science 372 (2021) 6547.
[33] N.C. Frey, J. Wang, G.I. Vega Bellido, et al., ACS Nano 13 (2019) 3031–3041.
[34] M. Naguib, V.N. Mochalin, M.W. Barsoum, Y. Gogotsi, Adv. Mater. 26 (2014) 992–1005.
[35] B. Anasori, M.R. Lukatskaya, Y. Gogotsi, et al., Nat. Rev. Mater. 2 (2017) 16098.
[36] J.F. Li, L. Han, Y.Q. Li, et al., Chem. Eng. J. 380 (2020) 122590.
[37] M.A. Saeed, A. Shahzad, K. Rasool, et al., Adv. Sci. 9 (2022) 2104743.
[38] F. Zhang, Y. Zhou, Y. Zhang, D. Li, Z. Huang, Nanophotonics 9 (2020) 2025–2032.
[39] P. Zhang, D. Wang, Q. Zhu, et al., Nanomicro. Lett. 11 (2019) 81.
[40] K. Huang, Z. Li, J. Lin, G. Han, P. Huang, Chem. Soc. Rev. 47 (2018) 5109–5124.
[41] F. Damiri, M.H. Rahman, M. Zehravi, et al., Materials 15 (2022) 1666.
[42] T. Yaqoob, M. Rani, A. Mahmood, et al., Materials 14 (2021) 6008.
[43] H. Pazniak, A.S. Varezhnikov, D.A. Kolosov, et al., Adv. Mater. 33 (2021) 2104878.
[44] X. Zhan, C. Si, J. Zhou, Z. Sun, Nanoscale Horiz. 5 (2020) 235–258.
[45] B. Anasori, Y. Xie, M. Beidaghi, et al., ACS Nano 9 (2015) 9507–9516.
[46] A. Lipatov, H. Lu, M. Alhabeb, et al., Sci. Adv. 4 (2018) eaat0491.

[47] K.L. Firestein, J.E. von Treifeldt, D.G. Kvashnin, et al., Nano Lett. 20 (2020) 5900–5908.
[48] T. Hu, J. Yang, W. Li, X. Wang, C.M. Li, Phys. Chem. Chem. Phys. 22 (2020) 2115–2121.
[49] J.C. Lei, X. Zhang, Z. Zhou, Front. Phys. 10 (2015) 276–286.
[50] R.M. Ronchi, J.T. Arantes, S.F. Santos, Ceram. Int. 45 (2019) 18167–18188.
[51] M. Naguib, O. Mashtalir, J. Carle, et al., ACS Nano 6 (2012) 1322–1331.
[52] Y. Wei, P. Zhang, R.A. Soomro, Q. Zhu, B. Xu, Adv. Mater. 33 (2021) 2103148.
[53] V. Kamysbayev, A.S. Filatov, H. Hu, et al., Science 369 (2020) 979–983.
[54] T. Zhang, L. Chang, X. Zhang, et al., Nat. Commun. 13 (2022) 6731.
[55] M. Naguib, M. Kurtoglu, V. Presser, et al., Adv. Mater. 23 (2011) 4248–4253.
[56] X.S. Zou, H. Liu, H. Xu, et al., Mater. Today Energy 20 (2021) 100668.
[57] J.F. Zhou, S. Lin, Y.N. Huang, et al., Chem. Eng. J. 373 (2019) 203–212.
[58] F.F. Liu, J. Zhou, S.W. Wang, et al., J. Electrochem. Soc. 164 (2017) A709–A713.
[59] M. Ghidiu, M. Naguib, C. Shi, et al., Chem. Commun. 50 (2014) 9517–9520.
[60] G. Deysher, C.E. Shuck, K. Hantanasirisakul, et al., ACS Nano 14 (2020) 204–217.
[61] M. Alhabeb, K. Maleski, B. Anasori, et al., Chem. Mater. 29 (2017) 7633–7644.
[62] X.H. Sang, Y. Xie, M.W. Lin, et al., ACS Nano 10 (2016) 9193–9200.
[63] M. Naguib, J. Halim, J. Lu, et al., J. Am. Chem. Soc. 135 (2013) 15966–15969.
[64] H. Cheng, W. Zhao, Friction 10 (2021) 398–410.
[65] D. Music, Z. Sun, A.A. Voevodin, J.M. Schneider, Solid State Commun. 139 (2006) 139–143.
[66] S. Neampet, N. Ruecha, J. Qin, et al., Microchim. Acta 186 (2019) 752.
[67] M. Ghidiu, M.R. Lukatskaya, M.Q. Zhao, Y. Gogotsi, M.W. Barsoum, Nature 516 (2014) 78–81.
[68] A. Lipatov, M. Alhabeb, M.R. Lukatskaya, et al., Adv. Electron. Mater. 2 (2016) 1600255.
[69] F.F. Liu, A.G. Zhou, J.F. Chen, et al., Appl. Sur. Sci. 416 (2017) 781–789.
[70] J. Halim, M.R. Lukatskaya, K.M. Cook, et al., Chem. Mater. 26 (2014) 2374–2381.
[71] S. Kim, J. Lee, S. Doo, et al., ACS Appl. Nano Mater. 4 (2021) 14249–14257.
[72] V. Natu, R. Pai, M. Sokol, et al., Chem 6 (2020) 616–630.
[73] P. Urbankowski, B. Anasori, T. Makaryan, et al., Nanoscale 8 (2016) 11385–11391.
[74] M. Li, J. Lu, K. Luo, et al., J. Am. Chem. Soc. 41 (2019) 4730–4737.
[75] Y. Li, H. Shao, Z. Lin, et al., Nat. Mater. 19 (2020) 894–899.
[76] S. Yang, P. Zhang, F. Wang, et al., Angew. Chem. Int. Ed. Engl. 57 (2018) 15491–15495.
[77] C. Wang, H. Shou, S. Chen, et al., Adv. Mater. 33 (2021) 2101015.
[78] A. Jawaid, A. Hassan, G. Neher, et al., ACS Nano 15 (2021) 2771–2777.
[79] D.H. Ho, Y.Y. Choi, S.B. Jo, J.M. Myoung, J.H. Cho, Adv. Mater. 33 (2021) 2005846.
[80] Y. Lee, S.J. Kim, Y.J. Kim, et al., J. Mater. Chem. A 8 (2020) 573–581.
[81] V. Natu, J.L. Hart, M. Sokol, et al., Angew. Chem. Int. Ed. 58 (2019) 12655–12660.
[82] X. Zhang, X. Liu, Y. Feng, et al., Appl. Mater. Today 27 (2022) 101483.
[83] T.S. Mathis, K. Maleski, A. Goad, et al., ACS Nano 15 (2021) 6420–6429.
[84] S.H. Lee, W. Eom, H. Shin, et al., ACS Appl. Mater. Interfaces 12 (2020) 10434–10442.
[85] B. Sun, H. Lv, Z. Liu, J. Wang, K. Shi, J. Mater. Chem. A 9 (2021) 6335–6344.
[86] T. Thomas, J. Ramón, V. Agarwal, et al., Microporous Mesoporous Mater. 336 (2022) 111872.
[87] S. Wang, Y. Jiang, B. Liu, et al., Sens. Actuator. B: Chem. 343 (2021) 130069.
[88] X. Wang, K. Sun, K. Li, et al., Chin. Chem. Lett. 31 (2020) 1018–1021.
[89] M. Wu, M. He, Q. Hu, Q. Wu, A. Zhou, ACS Sens. 4 (2019) 2763–2770.
[90] W.N. Zhao, N. Yun, Z.H. Dai, Y.F. Li, RSC Adv. 10 (2020) 1261–1270.
[91] Z.J. Yang, L. Jiang, J. Wang, et al., Sens. Actuator. B: Chem. 326 (2020) 128828.
[92] M. Kurtoglu, M. Naguib, Y. Gogotsi, M.W. Barsoum, MRS Commun. 2 (2012) 133–137.
[93] M. Khazaei, M. Arai, T. Sasaki, et al., Adv. Funct. Mater. 23 (2013) 2185–2192.
[94] X.F. Yu, Y.C. Li, J.B. Cheng, et al., ACS Appl. Mater. Interfaces 7 (2015) 13707–13713.
[95] J. Wang, R.Q. Xu, Y. Xia, S. Komarneni, Ceram. Int. 47 (2021) 34437–34442.
[96] E. Lee, A. VahidMohammadi, B.C. Prorok, et al., ACS Appl. Mater. Interfaces 9 (2017) 37184–37190.
[97] S.J. Kim, H.J. Koh, C.E. Ren, et al., ACS Nano 12 (2018) 986–993.
[98] C.E. Shuck, M.K. Han, K. Maleski, et al., ACS Appl. Nano Mater. 2 (2019) 3368–3376.
[99] Z. Yang, H. Zou, Y. Zhang, et al., Adv. Funct. Mater. 32 (2022) 2108959.
[100] S.J. Kim, J. Choi, K. Maleski, et al., ACS Appl. Mater. Interfaces 11 (2019) 32320–32327.
[101] H.J. Koh, S.J. Kim, K. Maleski, et al., ACS Sens. 4 (2019) 1365–1372.
[102] K. Liang, R.A. Matsumoto, W. Zhao, et al., Adv. Funct. Mater. 31 (2021) 2104007.
[103] S. Thomas, M.A. Zaeem, Adv. Theory 4 (2021) 2000250.
[104] E. Lee, A. VahidMohammadi, Y.S. Yoon, M. Beidaghi, D.J. Kim, ACS Sens. 4 (2019) 1603–1611.
[105] W. Guo, S.G. Surya, V. Babar, F. Ming, K.N. Salama, ACS Appl. Mater. Interfaces 12 (2020) 57218–57227.
[106] C. Hu, X. Yu, Y. Li, J. Cheng, B. Xiao, Appl. Surf. Sci. 607 (2023) 155104.
[107] S.R. Naqvi, V. Shukla, N.K. Jena, W. Luo, R. Ahuja, Appl. Mater. Today 19 (2020) 100574.
[108] M. Donarelli, L. Ottaviano, Sensors 18 (2018) 3638.
[109] A. Shokri, N. Salami, Sens. Actuator. B: Chem. 236 (2016) 378–385.
[110] J.F. Li, L. Han, X.L. Zhang, et al., Chem. Eng. J. 406 (2021) 126873.
[111] V. Le, Y. Vasseghian, V. Doan, et al., Chemosphere 291 (2022) 133025.
[112] Y. Xia, S.F. He, J.M. Wang, et al., Chem. Commun. 57 (2021) 9136–9139.
[113] W.Y. Chen, X.F. Jiang, S.N. Lai, D. Peroulis, L. Stanciu, Nat. Commun. 11 (2020) 1302.
[114] M. Liu, Z.Y. Wang, P. Song, Z.X. Yang, Q. Wang, Ceram. Int. 47 (2021) 23028–23037.
[115] C. Wang, R. Li, L. Feng, J. Xu, Chemosensors 10 (2022) 109.
[116] S.B. Sun, M.W. Wang, X.T. Chang, et al., Sens. Actuator. B: Chem. 304 (2020) 127274.
[117] J. Choi, Y.J. Kim, S.Y. Cho, et al., Adv. Funct. Mater. 30 (2020) 2003998.
[118] S.W. Liu, M.Y. Wang, G.W. Liu, et al., Appl. Sur. Sci. 567 (2021) 150747.
[119] N.M. Tran, Q.T.H. Ta, J.S. Noh, Mater. Chem. Phys. 273 (2021) 125087.
[120] S. Kumar, V. Pavelyev, P. Mishra, N. Tripathi, Sens. Actuator. A: Phys. 283 (2018) 174–186.
[121] L.J. Zhao, Y.Q. Zheng, K. Wang, et al., Adv. Mater. Technol. 5 (2020) 200248.
[122] S. Wang, Y.D. Jiang, B.H. Liu, et al., Sens. Actuator. B: Chem. 343 (2021) 130069.
[123] S. Wang, B.H. Liu, Z.H. Duan, et al., Sens. Actuator. B: Chem. 327 (2021) 128923.
[124] P. Chen, Z.H. Zhao, Z.G. Shao, et al., J. Mater. Sci. Mater. Electron. 33 (2022) 6168–6177.
[125] L. Jin, C.L. Wu, K. Wei, et al., ACS Appl. Nano Mater. 3 (2020) 12071–12079.
[126] Y. Zhou, Y.H. Wang, Y.J. Wang, X. Li, Anal. Chem. 92 (2020) 16033–16042.
[127] X. Li, J.L. Xu, Y.D. Jiang, et al., Sens. Actuator. B: Chem. 316 (2020) 128144.
[128] X.N. Wu, Y.J. Gong, B.J. Yang, et al., Appl. Surf. Sci. 581 (2022) 152364.
[129] M. Liu, Z.Y. Wang, P. Song, Z.X. Yang, Q. Wang, Sens. Actuator. B: Chem. 340 (2021) 129946.
[130] F. Ranjbar, S. Hajati, M. Ghaedi, et al., J. Hazard. Mater. 416 (2021) 126196.
[131] R. Bhardwaj, A. Hazra, J. Mater. Chem. C 9 (2021) 15735–15754.
[132] M. Wu, Y. An, R. Yang, et al., ACS Appl. Nano Mater. 4 (2021) 6257–6268.
[133] E. Lee, Y.S. Yoon, D.J. Kim, ACS Sens. 3 (2018) 2045–2060.
[134] U.T. Nakate, R. Ahmad, P. Patil, Y.T. Yu, Y.B. Hahn, Appl. Surf. Sci. 506 (2019) 144971.
[135] P.G. Choi, N. Izu, N. Shirahata, Y. Masuda, Sens. Actuator. B: Chem. 296 (2019) 126655.
[136] M. Al-Hashem, S. Akbar, P. Morris, Sens. Actuator. B: Chem. 301 (2019) 126845.
[137] Y.J. Kwon, H.W. Kim, W.C. Ko, et al., J. Mater. Chem. A 7 (2019) 27205–27211.
[138] Z. Li, X. Liu, M. Zhou, et al., J. Hazard. Mater. 415 (2021) 125757.
[139] J. Wu, Q. Huang, D. Zeng, et al., Sens. Actuator. B: Chem. 198 (2014) 62–69.
[140] Y. Xu, L. Zheng, C. Yang, et al., ACS Appl. Mater. Interfaces 12 (2020) 20704–20713.
[141] S. Gasso, M.K. Sohal, A. Mahajan, Sens. Actuator. B: Chem. 357 (2022) 131427.
[142] H. Yan, L. Chu, Z. Li, et al., Sens. Actuator. Rep. 4 (2022) 100103.